JOURNAL OF GEOPHYSICAL RESEARCH, VOL. , NO. , PAGES 1–8,

Equatorial model of subauroral polarization stream

J. Goldstein[1], J. L. Burch[1], B. R. Sandel[2]

Abstract.
We present an equatorial model of the subauroral polarization stream (SAPS) electric potential, parameterized by K_p index (valid for $K_p = 4$–7), based on a previous study of the average characteristics of SAPS. The model treats the SAPS westward flow channel as a negative potential drop whose radial location and width decrease as a function of both increasing magnetic local time (MLT) and increasing K_p. The magnitude of the SAPS potential drop decreases eastward across the nightside, and increases with increasing K_p. The model SAPS flow channel significantly alters the flow paths of plasma in the afternoon and evening MLT sectors, and agrees with an earlier study that used an ad-hoc SAPS potential to obtain good agreement with plasmasphere observations. The model performance is tested via comparison with 13 intervals of plasmapause data obtained during the period 1 April through 31 May 2001 by the extreme ultraviolet (EUV) imager on the Imager for Magnetopause-to-Aurora Global Exploration (IMAGE) satellite. Although the model performs well, the current K_p-based parameterization is somewhat crude, capturing only the gross spatial and temporal SAPS characteristics. Future SAPS models should rely on a more thorough study of the average characteristics of SAPS to constrain/parameterize the functional form better.

1. Subauroral Polarization Stream (SAPS)

It is well established that during intervals of southward interplanetary magnetic field (IMF), dayside magnetopause reconnection (DMR) drives a two-cell convection pattern in which outer magnetospheric (high ionospheric latitude) plasma is dragged antisunward and inner magnetospheric (low-latitude) plasma moves sunward [*Dungey*, 1961]. Numerous studies have shown that the strength of DMR-driven sunward convection exerts a primary influence on the dynamics and structure of the plasmasphere, the cold, rotating torus of plasma that encircles the Earth [*Carpenter and Lemaire*, 1997; *Lemaire and Gringauz*, 1998]. Although the zero-order, global active-time plasmaspheric dynamics are adequately described by the DMR-driven convection hypothesis, this simple picture is clearly incomplete [*Goldstein and Sandel*, 2005].

A significant modification of DMR-driven convection is a phenomenon that has come to be called the subauroral polarization stream (SAPS) [*Foster and Burke*, 2002]. SAPS is a disturbance-time effect in which feedback between the ring current and ionosphere produces an intense, radially narrow, westward flow channel, mainly in the dusk-to-midnight magnetic local time (MLT) sector [*Burke et al.*, 1998; *Foster and Vo*, 2002]. The SAPS effect arises from a global electrical current circuit and feedback effect involving the partial ring current (RC), region 1 (R1) and region 2 (R2) field aligned currents (FAC), and poleward Pedersen currents in the ionosphere. Region 2 FAC (present at RC pressure gradients) flow down into the subauroral evening-MLT ionosphere and feed into Pedersen currents that flow poleward to connect with the region 1 auroral FAC. Because of the low ionospheric conductivity at subauroral latitudes, the poleward Pedersen currents generate intense poleward electric (E) fields in the region between the R2 FAC and the low-latitude edge of the electron aurora. The presence of the poleward E-fields also further reduces the ionospheric conductivity, intensifying the E-fields and creating a very narrow peak that often occupies the low-latitude edge of the broader SAPS region. This intense, narrow peak is known as subauroral ion drift (SAID) [*Anderson et al.*, 2001]. The poleward ionospheric SAPS E-fields map to the equatorial plane as radial E-fields, i.e., westward flows. This equatorial westward flow channel is the focus of our paper.

Because of the ring-current/ionosphere feedback involved in SAPS generation, the IMF polarity at the magnetopause does not directly turn SAPS on and off as it does DMR convection; SAPS can persist even when DMR-driven convection has subsided following a northward IMF turning. SAPS has been demonstrated to modify plasmasphere dynamics in the dusk-to-midnight sector by intensifying sunward convection, thus sharpening the outer radial density gradient at the plasmapause boundary, smoothing the MLT shape of the plasmapause, and at times creating narrow duskside plumes that are distinct from the broad dayside plumes created from more global DMR-driven convection [*Goldstein et al.*, 2003b; *Goldstein and Sandel*, 2005]. To properly model plasmaspheric dynamics in the evening sector where SAPS plays a crucial role, the SAPS effect must be considered as a process distinct from DMR-driven convection. Currently, there is no general-use parameterized equatorial model for the electric potential associated with SAPS. The average spatial and temporal properties of ionospheric SAPS have been roughly

[1] Space Science and Engineering Division, Southwest Research Institute, San Antonio, TX 78228 USA
[2] Lunar and Planetary Laboratory, University of Arizona, Tucson, AZ 85721 USA

Paper number .
0148-0227/05/$9.00

characterized as a function of magnetic latitude (MLAT), MLT, and the geomagnetic activity index K_p [*Foster and Vo*, 2002]. *Goldstein et al.* [2003b] used an ad-hoc functional form for an equatorial SAPS potential to obtain good model performance for a single event study. In this paper, we present an equatorial SAPS model potential based on the functional form of the ad-hoc model of *Goldstein et al.* [2003b], constrained by the parameterization of *Foster and Vo* [2002].

2. Equatorial SAPS Model

From *Foster and Vo* [2002] (hereinafter called FV02), the SAPS flow channel has the following average properties in the ionosphere. (1) On the nightside the latitude of the peak of the SAPS flow stream decreases uniformly as a function of both MLT and increasing K_p index. (2) The latitudinal width of the SAPS flow channel decreases from 3–5° at 2200 MLT to 3° at 0300 MLT. (3) The magnitude of SAPS decreases eastward across the nightside. (4) The magnitude of SAPS flows increases with K_p. Our model will quantitatively include each of these properties.

Following *Goldstein et al.* [2003b] (hereinafter called G03), we model SAPS as an equatorial electric potential

$$\Phi_{\mathrm{S}}(r,\varphi,t) = -F(r,\varphi)\ G(\varphi)\ V_{\mathrm{S}}(t)\ . \tag{1}$$

This Φ_{S} consists of a dimensionless spatial component $-F(r,\varphi)\ G(\varphi)$ and a time-dependent magnitude $V_{\mathrm{S}}(t)$ of the electric potential. We first discuss the spatial part.

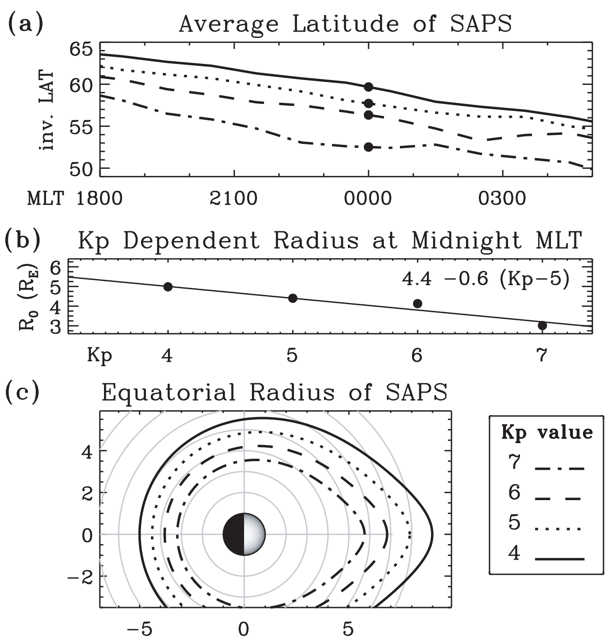

Figure 1. (a) Average invariant magnetic latitude of SAPS, plotted versus MLT for four values of K_p (4, 5, 6, and 7). Adapted from Figure 3 of *Foster and Vo* [2002]. Dots indicate SAPS latitude locations at midnight (0000) MLT (see (b)). (b) K_p-dependent radius of SAPS at 0000 MLT. Dots: SAPS latitudes at 0000 MLT (from Figure 1a), mapped to the magnetic equator using the T89 model. Line: Linear fit to four mapped points (c) Equatorial radius of SAPS (Equations (3) and (4)) for four K_p values. The Sun is to the right; circles drawn at integer L values.

2.1. Radial Dependence

For the radial dependence we use the function

$$F(r,\varphi) = \frac{1}{2} + \frac{1}{\pi}\tan^{-1}\left[\frac{2}{\alpha}\{r - R_{\mathrm{S}}(\varphi)\}\right]. \tag{2}$$

The function $-F(r,\varphi)$ treats the SAPS flow channel as a potential drop (i.e., potential decreasing with r) centered at radius R_{S}, corresponding to a peak in radial E-field (i.e., westward flow) at R_{S}, with the width of the peak given by α. Parameterizations of R_{S} and α are given in the next two subsections.

2.2. Radial Location

From the list of SAPS properties above, (1) the nightside latitude of SAPS decreases uniformly as a function of both MLT and increasing K_p index. In Figure 1a, the invariant latitude of SAPS is plotted versus MLT, for four K_p values as given by the legend in the lower right corner of Figure 1. In the equatorial plane, the MLT dependence of the SAPS latitude corresponds to a radial SAPS location R_{S} that decreases eastward across the nightside. Following G03, we model the SAPS radial location as

$$R_{\mathrm{S}}(\varphi) = R_0\left[\frac{1+\beta}{1+\beta\cos(\varphi-\pi)}\right]^{\kappa}, \tag{3}$$

with $\beta = 0.97$ and $\kappa = 0.14$. To fully specify R_{S} requires R_0, the SAPS radial location at midnight MLT (i.e., $\varphi = \pi$). The SAPS latitude at midnight MLT (taken from Figure 1a) was mapped to the magnetic equator for four K_p values using the Tsyganenko (T89) field [*Tsyganenko*, 1989]. Because the published data of FV02 do not contain date or time information needed to model the tilt angle of the intrinsic dipole field, we assumed zero dipole tilt in the T89 mapping. Even with this simple assumption, the T89 model is

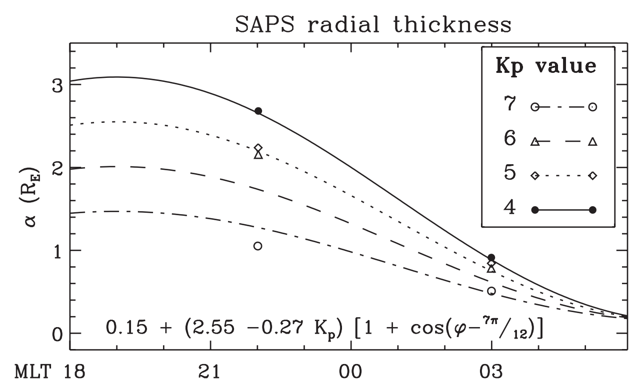

Figure 2. Thickness of SAPS flow channel versus MLT and K_p (see legend). Individual points: latitudinal SAPS thicknesses mapped to magnetic equator using T89. Lines: cosine fit to individual points, given by equation at bottom of plot.

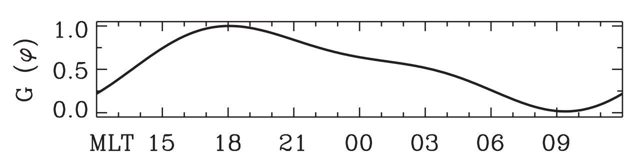

Figure 3. Azimuthal dependence $G(\varphi)$ of the magnitude of the SAPS potential.

in principle more realistic than a dipole field (which ignores the magnetic distortion associated with the partial RC pressure buildup necessary for SAPS). The four mapped values of SAPS radial location are plotted versus K_p in Figure 1b. We fit a line to these four values:

$$R_0 = 4.4 R_{\mathrm{E}} - 0.6\,(K_p - 5) \tag{4}$$

Figure 1c plots R_{S} for four K_p values. Consistent with average SAPS properties, the SAPS location moves inward (earthward) with increasing K_p, and with increasing MLT across the nightside between dusk and midnight MLT. East of midnight our function R_{S} fails to capture the precise shape of the SAPS radial location, but because the peak SAPS strength occurs near dusk (as explained later in the $G(\varphi)$ discussion), the dawnside shape of R_{S} is less important in terms of overall model performance.

2.3. Radial Width

The radial electric field associated with the potential $-F(r,\varphi)$ is $\partial F/\partial r$, which has a peak value $2/(\pi\alpha)$ at $r = R_{\mathrm{S}}$, and decreases to 0.5 of its peak value at $r = R_{\mathrm{S}} \pm 0.5\alpha$. Figure 4 of FV02 (not reproduced here) contains histograms of SAPS region widths (in degrees latitude) at two MLT locations. Taking weighted averages of these 2 histograms gives ionospheric SAPS widths $\Delta\Lambda$ equal to $4.11°\Lambda$ at 2200 MLT and $3.31°\Lambda$ at 0300 MLT. Assuming these latitudinal SAPS widths are centered at the latitudinal locations of SAPS plotted in Figure 1, we mapped them to the magnetic equator using the T89 model, producing the grouped points plotted at 2200 MLT and 0300 MLT in Figure 2. To model these points we assumed a cosine variation with a maximum at 1900 MLT (i.e., $\varphi = 7\pi/12$):

$$\alpha = 0.15 + (2.55 - 0.27 K_p)\left[1 + \cos(\varphi - \frac{7\pi}{12})\right]. \tag{5}$$

This function is plotted for four K_p values in Figure 2.

2.4. Azimuthal Modulation of SAPS Magnitude

The magnitude of the SAPS potential drop decreases eastward across the nightside, as given by Figure 7 of FV02 (not reproduced here). Based on this published figure, we model the azimuthal dependence of the potential drop (normalized to the maximum at a given K_p) as

$$G(\varphi) = \sum_{m=0}^{2} \{A_m \cos[m(\varphi - \varphi_0)] + B_m \sin[m(\varphi - \varphi_0)]\}$$

where $\varphi_0 = 7\pi/12$, $A_m = [53, 37, 10]/100$, and $B_m = [0, 21, -10]/100$. As shown in Figure 3, this function is periodic in φ (i.e., MLT), with a maximum at 1900 MLT and a minimum at 1024 MLT. Because of the pre-noon minimum in $G(\varphi)$, the SAPS potential is negligible in most of this MLT sector.

2.5. Time Dependence of SAPS

The time dependence of our equatorial SAPS potential (Equation (1)) is contained in $V_{\mathrm{S}}(t)$. Since our model is based solely on the average SAPS characteristics (versus K_p) determined by FV02, our function V_{S} will depend explicitly on K_p, with the time dependence implicit in K_p. Figure 7 of FV02 (not reproduced here) contains average SAPS potential distributions for $K_p = 4, 6, 7$, and > 7. From each of the FV02 potential plots we determined the peak value of electric potential; these are plotted in Figure 4 as vertical error bars. To fit these four data points, we use the simple function

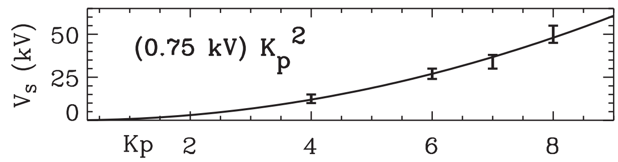

Figure 4. K_p dependence of the magnitude V_{S} of the SAPS potential.

$$V_{\mathrm{S}} = (0.75\mathrm{kV})\; K_p^2. \tag{6}$$

3. Model Use and Performance

Goldstein et al. [2003b] (G03) showed that the sunward convection arising from dayside magnetopause reconnection (DMR) and SAPS need to be modeled as two distinct processes, the former due to external (solar wind) influence and the latter due to internal processes (coupling between the ring current and ionosphere). Therefore, the SAPS model described in this paper is intended to be used in conjunction with a separate model that treats the DMR-driven convection. A simple and popular DMR-driven convection model is the shielded convection potential of *Volland* [1973] and *Stern* [1975]:

$$\Phi_{\mathrm{VS}} = -A\, r^2 \sin\varphi. \tag{7}$$

This model is not necessarily the most realistic, but if properly normalized to the solar wind electric field it is a good

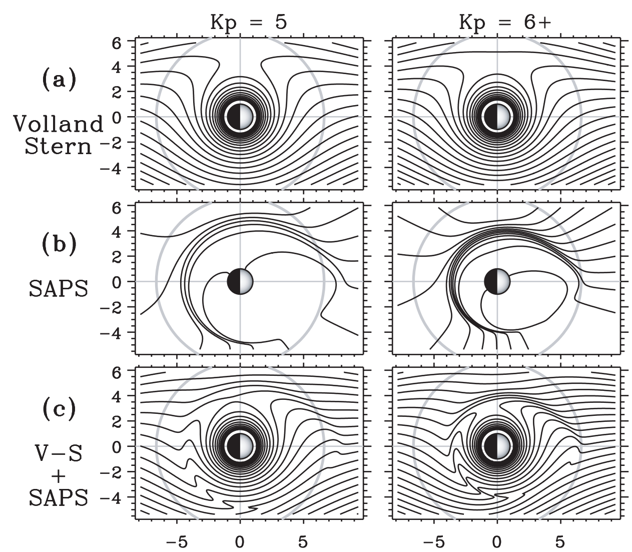

Figure 5. Equatorial SAPS potential model for $K_p = 5$ (left column) and $K_p = 6^+$ (right column). In each plot the Earth is in the center and the Sun is to the right. A gray circle is drawn at geosynchronous orbit (6.62 R_{E}). (a) Volland-Stern model plus corotation (4 kV potential spacing); note large flow stagnation region near dusk. (b) SAPS model (2.5 kV spacing), a narrow westward flow channel. (c) SAPS added to Figure 5a (4 kV spacing); duskside sunward flows are significantly enhanced.

representation of the DMR-driven convection paradigm. A commonly used normalization of the coefficient A is that of *Maynard and Chen* [1975]:

$$A_{\mathrm{MC}} = \frac{0.045}{1 - 0.159\,K_p + 0.0093\,{K_p}^2} \quad (\mathrm{kV}/R_{\mathrm{E}}^2). \qquad (8)$$

Figure 5 shows how the SAPS model can be added to a DMR convection model to produce a potential function that represents both external (solar wind driven) and internal (coupling driven) convection. Figure 5a shows the Volland-Stern potential using the A_{MC} normalization for $K_p = 5$ and $K_p = 6^+$. Added to corotation, the Volland-Stern model gives a large duskside region of flow stagnation. Figure 5b plots the full SAPS model of Equation (1). The closely spaced equipotentials (flow streamlines) occur inside the westward SAPS flow channel. Note that the $K_p = 5$ model in Figure 5b agrees well with the ad-hoc SAPS model potential (optimized for a single $K_p = 5$ event, as described below) that is plotted in Figure 3 of G03 (not reproduced here). Figure 5c shows that when added to the Volland-Stern model of Figure 5a, the SAPS flow channel significantly enhances the sunward flow component on the duskside, as intended. In the post-noon MLT sector, the SAPS effect bends flow streamlines in the $-Y$ direction. The SAPS model also modifies the premidnight MLT sector by weakening the roughly eastward convective flows, creating kinks in the streamlines there. In the pre-noon MLT sector, the SAPS model effect is negligible.

3.1. Model Validation Methodology

To validate the SAPS model, we performed two tests in which the model was used to create simulated plasmapauses that were compared with observations. The first test is a case study of a single event (2 June 2001) and the second test is a semi-statistical study of 13 events from 1 April through 31 May 2001.

3.1.1. Plasmapause Test Particle (PTP) Code.

We simulate the plasmapause boundary as a series of cold test particles subject only to $E \times B$ drift. In this "plasmapause test particle" (PTP) simulation, the plasmapause evolution is modeled by the changing shape of the curve defined by the aggregate of the test particles that move in response to a time-varying electric potential. Plasmapause test particles are added and/or removed as necessary to resolve the plasmapause curve, using the constraint that the inter-particle distance is within the range 0.05–0.4 R_{E}. The time resolution of the simulation is 30 seconds. To represent DMR-driven convection, we use the Volland-Stern (VS) model discussed earlier. Although in Figure 5 it was convenient to use the K_p-based normalization A_{MC}, for the PTP simulations we follow G03 and instead use

$$A = 0.12\,E_{\mathrm{SW}}\,(6.6\,R_{\mathrm{E}})^{-1}, \qquad (9)$$

equivalent to 12 percent of the solar wind E-field applied inside geosynchronous orbit. As explained by G03, this approach allows the reconnection-driven component of convection to be treated as a process separate from SAPS. The dawn-to-dusk solar wind E-field is calculated as $E_{\mathrm{SW}} = -V_{\mathrm{SW}} B_{z,\mathrm{SW}}$, with the constraint $E_{\mathrm{SW}} \geq 0.1$ mV/m. Here V_{SW} is the magnitude of the solar wind bulk flow speed and $B_{z,\mathrm{IMF}}$ is the north-south component of the interplanetary magnetic field (IMF), both measured by the Advanced Composition Explorer (ACE) spacecraft [*Stone et al.*, 1998].

3.1.2. Global EUV Plasmasphere Images.

The observations consist of global plasmasphere images obtained by the extreme ultraviolet (EUV) imager on the Imager for Magnetopause-to-Aurora Global Exploration (IMAGE) satellite [*Sandel et al.*, 2001]. The EUV imager detects 30.4 nm light resonantly scattered by plasmaspheric He^+ ions, providing full global images of the high-density plasmasphere (above about 40 e$^-$ cm^{-3}) at a nominal time cadence of 10 min and with nominal spatial resolution of $0.1R_{\mathrm{E}}$ or better [*Goldstein et al.*, 2003c].

Analysis of EUV plasmasphere images typically involves mapping the raw images to the SM-coordinate magnetic equatorial plane [*Roelof and Skinner*, 2000] and then manually extracting plasmapause locations from the 2D mapped images. These manually extracted plasmapauses can agree with simultaneous (or near-simultaneous) in situ data to within 0.2–0.4 R_{E} [*Goldstein et al.*, 2003c, 2004].

3.2. Test I: Single Event

The first test we performed was to reproduce the results of *Goldstein et al.* [2003b] (G03), in which an ad-hoc SAPS model was added to the Volland-Stern potential to drive a PTP simulation of an erosion event witnessed by IMAGE EUV during 0000–0500 UT on 2 June 2001. The ad-hoc SAPS model of G03 was specifically optimized to give good agreement with the 2 June 2001 IMAGE EUV plasmapause data, whereas our K_p-driven SAPS model is parameterized solely using average SAPS properties as reported by *Foster and Vo* [2002] (FV02). The 2 June 2001 erosion is therefore a

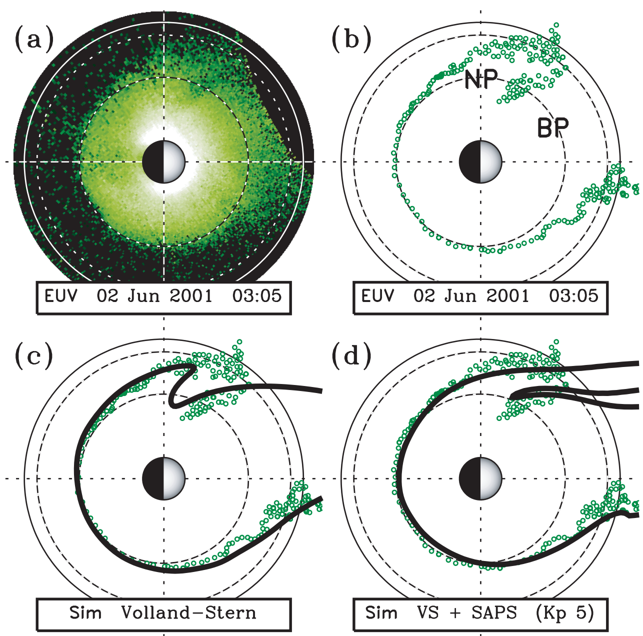

Figure 6. SAPS model performance for erosion event of 2 June 2001. (a) IMAGE EUV global snapshot of the plasmasphere, 0305 UT. The Earth is in the center; Sun to the right. Dotted circles at $L = 2$, 4. Solid circle at geosynchronous orbit ($L = 6.62$.) The plasmasphere is the green-white region surrounding the Earth out to $L = 4$ on the nightside. (b) Boundary points extracted from EUV image showing narrow duskside plume ("NP") and broad dayside plume ("BP"). (c) Plasmapause test particle (PTP) simulation using the Volland-Stern model. (d) PTP simultion with SAPS model added, showing proper formation of narrow duskside plume.

good case study to compare the new (K_p-based) model performance with the old. The calculation of E_{SW} from ACE data is not included here (see G03), but we note that the ACE data were time-delayed 55 min to account for propagation to the dayside magnetopause from ACE's upstream location. To account for a known (but as yet unexplained) delay between a southward IMF turning at the magnetopause and the subsequent commencement of plasmasphere erosion [*Goldstein et al.*, 2003a], the ACE data were delayed an additional 32 min. For the PTP simulation, we used the Volland-Stern potential (driven by the delayed E_{SW}), added to a corotation potential, plus the K_p-based SAPS model. As initial conditions for the simulation, we used an extracted EUV plasmapause from 0001 UT on 2 June, a time just before the erosion event began; our initial plasmapause is shown in Figure 2 of G03 (not reproduced here). Figure 6 shows the comparison between the PTP simulation and the IMAGE EUV data.

Figure 6a contains a global snapshot of the 2 June 2001 plasmasphere obtained at 0305 UT by the IMAGE EUV imager. Figure 6b plots points (green circles), manually extracted from the EUV image, that represent the plasmapause boundary. (For a full description of these extracted plasmapause points, see *Goldstein et al.* [2004].) As further described by G03, this 0305 UT EUV image was obtained in the middle of a plasmaspheric erosion. The erosion had moved the nightside plasmapause inward by about 2 R_{E}, to $L = 4$ (as shown in Figure 6b), and had created a broad dayside drainage plume (labeled "BP" in Figure 6b). Also discussed by G03, the SAPS flows present during this event created a narrow duskside plume (labeled "NP"), distinct from the broad dayside plume. This narrow duskside plume evolved when SAPS flows elongated the bulging eastern edge of an afternoon "notch" in the plasmapause. Similar SAPS-produced narrow plumes have been reported for other events [*Goldstein and Sandel*, 2005].

Figure 6c and Figure 6d overplot the PTP-simulated plasmapause (thick black line) onto the EUV plasmapause data (from Figure 6b). In Figure 6c the Volland-Stern (VS) model was used without the inclusion of SAPS. As found by G03, the EUV-observed nightside and dawnside plasmapause (green circles) are well modeled by the VS simulation (black curve), but west of the dusk terminator the VS simulation fails to reproduce the narrow duskside plume. Because of the large duskside stagnation point produced by the Volland-Stern potental (plus corotation), the duskside sunward flows are too weak, producing only a "horn"-like feature [*Goldstein et al.*, 2003b]. In Figure 6d the new SAPS model is added to the VS potential, preserving the good model performance on the nightside and dawnside, but enhancing the duskside sunward flows to produce the narrow duskside plume. Thus, the new K_p-based SAPS model produces a narrow plume that agrees with the EUV data, and the new model's performance is consistent with (and perhaps slightly better than) that of the ad-hoc SAPS model of G03.

3.3. Test II: April–May 2001

In the previous subsection we showed that our K_p-based SAPS model gave good agreement with observations of the 2 June 2001 erosion event. In this subsection we perform testing for a larger number of events. For this semi-statistical test, we selected the two-month period 1 April through 31 May 2001. Figure 7a is a plot of K_p during this two-month period. Yellow-colored portions of the plot (e.g., 1–2 April, 4–5 April, 8 April, etc.) show the 13 events selected for the SAPS model validation study. Our criterion for event selection was that each interval should contain some period during which K_p equaled or exceeded 4; the rationale for this criterion was that the SAPS model is only truly valid in the range K_p = 4–7. For reference, blue horizontal lines are drawn at K_p = 4, 5, 6, and 7. Vertical gray lines are drawn at 1-day intervals.

For these 13 selected events we analyzed 1547 EUV plasmasphere images, and extracted over 90,000 nightside plasmapause L values. These are represented by the plot in Figure 7b. Because of the large number of data, not all the individual plasmapause points are plotted. Each black dot is the average nightside plasmapause location from one EUV image (each image has, on average, 60 plasmapause points, distributed in MLT). The green (blue) dots are the per-image maximum (minimum) plasmapause locations.

As before, the PTP simulation electric field was calculated as the superposition of corotation, the Volland-Stern convection potential, and our K_p-based SAPS model. The Volland-Stern potential was normalized to the solar wind electric field according to Equation (9). The solar wind E-field measured by the ACE spacecraft (with a time delay to account for propagation to the magnetopause) is plotted in Figure 7c. For this 13-event-study we did not attempt to account for the delay (on average, 10–30 min) between an IMF polarity change at the magnetopause and a subsequent

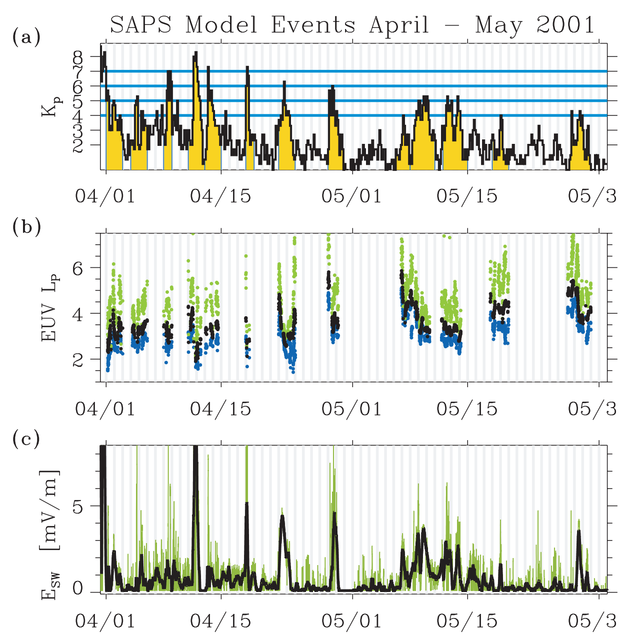

Figure 7. Summary of 13 events selected for validation of SAPS model. (a) K_p values, 1 April through 31 May 2001. Events selected for SAPS model validation are colored yellow. (b) Plasmapause L values extracted from 1547 IMAGE EUV images from the selected event intervals. Due to large volume of EUV plasmapause data (over 90,000 points), not all the individual points are plotted. Black dots show per-image average plasmapause. Green/blue dots are per-image maximum/minimum values. (c) Dawn-to-dusk solar wind electric field, 1 April - 31 May 2001, time delayed to account for propagation to the magnetopause. Green: 64-second averaged data. Black: 6-hour averaged data.

effect on the plasmasphere. The 6-hour averaged solar wind E-field (black line) is shown for reference, but the 64-second averaged data (green) were used in the actual simulation.

To model the selected events, 13 simulations were run. For each simulation, the initial plasmapause was specified using available IMAGE EUV plasmapause data. The initial plasmapauses for all 13 simulations are plotted in Figure 8.

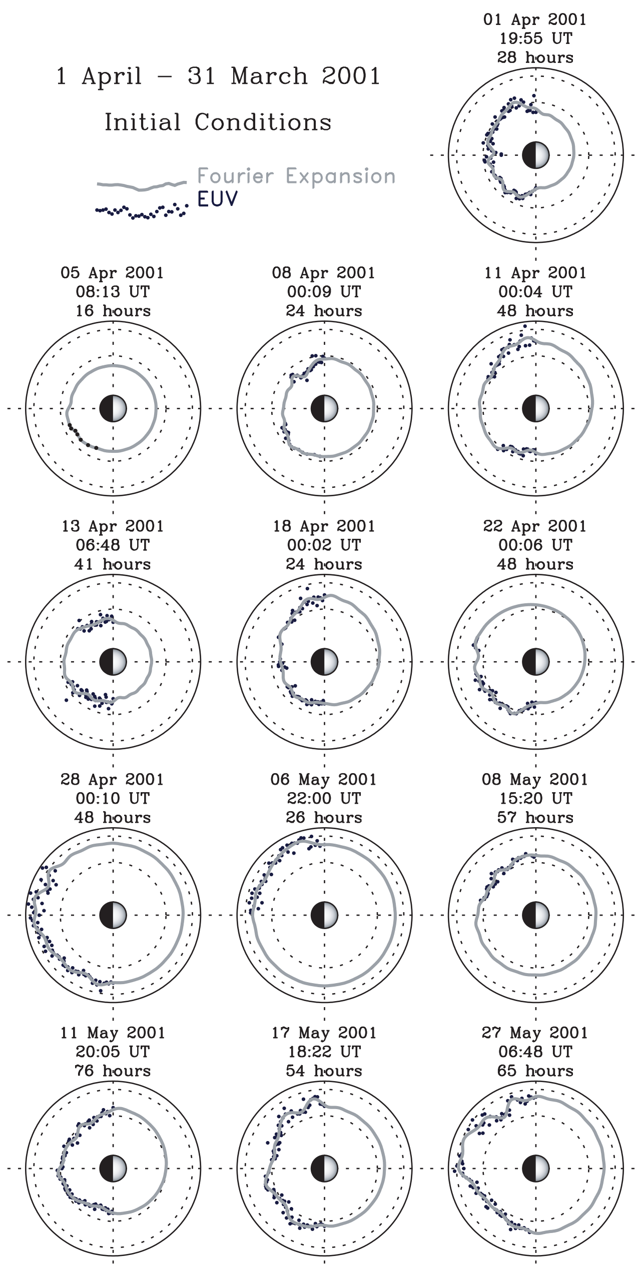

Figure 8. Initial conditions for 13 plasmapause test particle (PTP) simulations during the period 1 April–31 May 2001. Each plot corresponds to one PTP simulation, and is labeled at the top with date and time at which the simulation began, and the number of hours of simulation time that followed. In each plot, the Earth is in the center, with the Sun to the right. Dotted circles are drawn at $L = 4$ and $L = 6$; a solid circle is at geosynchronous orbit. The black dots show nightside plasmapause values extracted from an IMAGE EUV image at the date and time of the plot; the thick gray line is a Fourier series expansion of the EUV points.

The black dots are EUV plasmapause points; the thick gray line is the Fourier series expansion of the EUV points. For each simulation, a 200-point discretization of the Fourier expansion was used to specify the initial plasmapause. The initial date and time of each simulation, and the number of simulation hours, are indicated at the top of each plot.

Some snapshots from the 13 PTP simulations are shown in Figure 9; each plot is labeled with date, time, and K_p value. For each interval, the simulation was run both without the SAPS model (blue line), and with the SAPS model (red line). The black dots are the EUV plasmapause points. From the EUV data it is clear the plasmasphere at any given time does not depend upon instantaneous K_p value alone. For example, Figure 9c and Figure 9d are snapshots at the same K_p value (6^+), but in the latter plot the EUV plasmasphere (the region inside the plasmapause) is smaller. In fact it is known that the plasmasphere configuration arises due to a combination of prior conditions and the instantaneous geomagnetic activity level; longer, more intense storms produce

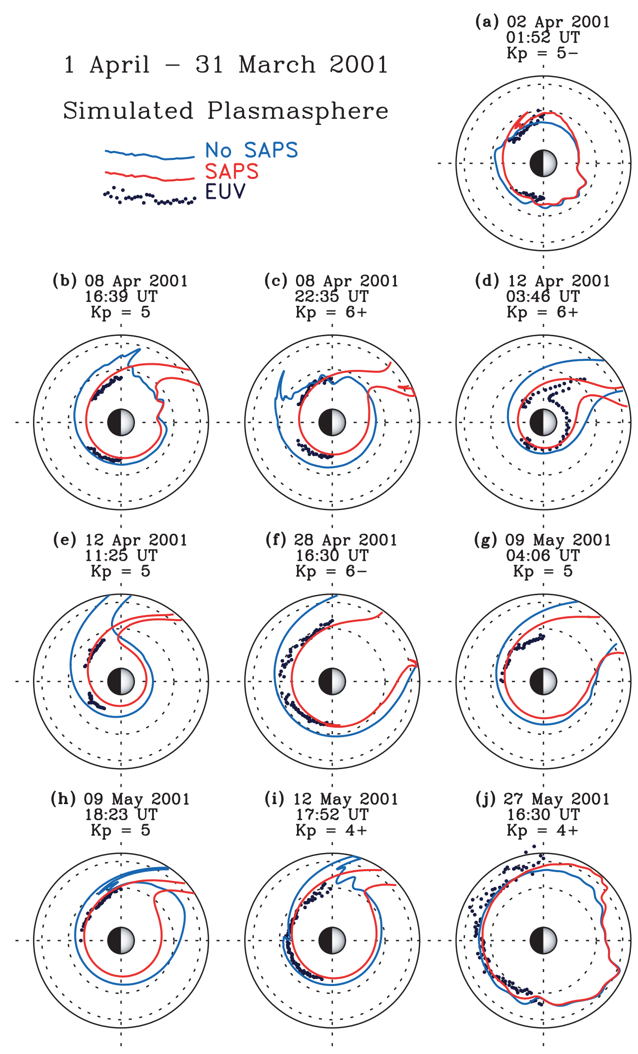

Figure 9. Snapshots of the results of the PTP simulations. The format is similar to that of Figure 8, except instead of Fourier expansions of the EUV data, simulated plasmapauses are plotted. The black dots are the EUV plasmapause data. The blue curve ("No SAPS") is the output of the simulation without the SAPS model. The red curve ("SAPS") shows the result of including the SAPS effect.

more extensive plasmasphere erosion. Therefore, our K_p-based SAPS model does not prescribe the plasmapause location, but rather specifies the properties of a SAPS-related electric field whose temporal and spatial variations cause the plasmapause to evolve.

The overall trend in Figure 9 is that inclusion of the SAPS model yields better duskside agreement. Near the duskside, the SAPS effect generally moves the plasmapause inward (at times creating a narrow duskside plume) so that it agrees better with the EUV plasmapause points. For example, in Figure 9b the blue curve ("No SAPS") lies about 1 R_E outside the red curve ("SAPS") near the dusk side, and the red curve agrees with the EUV data (black points) better. In Figure 9c, the SAPS effect produces a plume whose duskside edge lines up with the EUV data; without the SAPS effect, the simulation contains a rotating plume (at about 2200 MLT) that strongly disagrees with the data. In Figure 9d through Figure 9i, the simulation with the SAPS model produces a duskside plasmapause closer to the EUV data than the model without SAPS. In Figure 9j the SAPS model does not make a significant difference.

Our K_p-based SAPS model also moves the dawnside plasmapause inward. In some cases inclusion of the SAPS model yields a dawnside plasmapause that agrees better with the EUV data (e.g., Figure 9a and Figure 9d). In other cases, the SAPS effect moves the dawnside plasmapause inward too much (e.g., Figures 9b, 9e, and 9i).

Because the K_p-driven SAPS model has been parameterized based on average SAPS properties, it should not be expected to reproduce (for a given event) all of the spatial and temporal properties of the real SAPS effect. On average, however, the SAPS model should yield better agreement with the real plasmapause. This point is illustrated in the top plot of Figure 10a, the average plasmapause L value versus K_p, in the 2000–2200 MLT (pre-midnight) sector. To make this plot, we binned all the EUV data and all the PTP simulation output (for both cases, without and with SAPS)

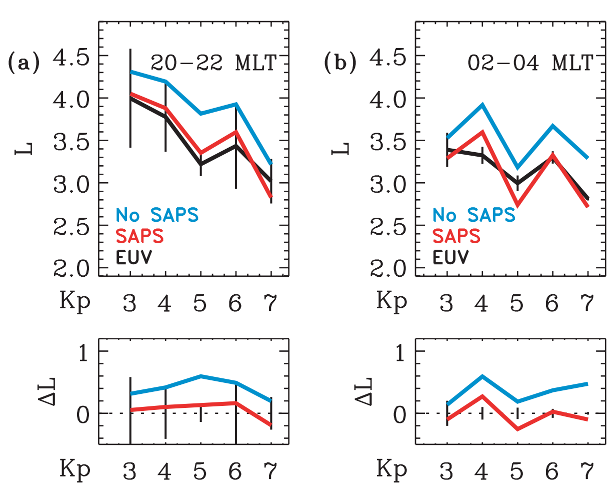

Figure 10. SAPS model performance for selected events during 1 April–31 May 2001 (see text), (a) 2000–2200 MLT and (b) 0200–0400 MLT. Black: IMAGE EUV plasmapause L with standard deviation error bars. Blue: Simulation results using Volland-Stern model alone. Red: simulation using Volland-Stern plus SAPS model, showing improved agreement with EUV data. The top plot shows the plasmapause L values; the bottom plot gives the difference between the simulation results and the EUV data.

into nearest-integer K_p bins between 3 and 7. (For example, the $K_p = 4$ bin includes $K_p = 4^-$, 4, and 4^+.) The thick black line plots the average pre-midnight EUV plasmapause for each K_p bin; as expected, the general trend is for the plasmapause to move inward with increasing geomagnetic activity (K_p). The black error bars give the standard deviation of the EUV plasmapause averages. The number of points in each average decreases with K_p, from almost 5000 points in the $K_p = 3$ bin to only 100 points in the $K_p = 7$ bin. Thus, at low K_p the uncertainty is mostly due to considerable scatter in the plasmapause location; at higher K_p the error bar reflects both scatter and low sample size. The thick blue (red) line gives the average plasmapause L value for the simulation without (with) SAPS included. The bottom plot of Figure 10a shows the L-value difference between each of the two simulations (without and with SAPS, blue and red, respectively) and the EUV average plasmapause. It is clear from Figure 10a that the agreement with the pre-midnight (2000–2200 MLT) EUV data is systematically better with SAPS included. The non-SAPS simulation overestimates the average pre-midnight plasmapause by about 0.2–0.5 R_E, whereas the SAPS simulation agrees with the EUV data to within 0.2 R_E. Note that for K_p between 4 and 7 (the range of validity of the SAPS model), the difference between the two simulations (SAPS and non-SAPS) equals or exceeds the uncertainty in the average EUV plasmapause L-values.

Figure 10b shows the same type of plots as Figure 10a, but in this case covering the 0200–0400 MLT (post-midnight) sector. As noted above in the discussion of Figure 9, in some cases inclusion of the SAPS model in the post-midnight sector helps the agreement with EUV data, but in other cases the SAPS effect moves the plasmapause inward too much. Nonetheless, the overall agreement is generally improved when using the SAPS model.

4. Discussion

The SAPS flow channel has a tangible effect on the location of the duskside plasmapause, and influences the precise location and shape of duskside plasmaspheric plumes. Plumes play an important (perhaps unique) role in magnetospheric dynamics. For example, plumes bring cold plasma into the outer magnetosphere, increasing the loss rate of the warmer particles of the ring current and radiation belts [*Spasojević et al.*, 2004; *Baker et al.*, 2004]. Therefore, proper modeling of the effect of SAPS on plumes is essential.

The SAPS effect arises when region 2 currents flow down into the low conductivity subauroral ionosphere, causing a poleward electric field in the subauroral region. An analytical model of SAPS should ideally be parameterized by either: (1) some measure of the strength of that poleward ionospheric electric field, or (2) an index related to the strength and latitude (relative to the equatorward edge of the aurora) of duskside region 2 currents. No routinely tabulated geomagnetic index directly fits either of these descriptions (1) or (2). The K_p index measures mid-latitude disturbance level in the form of a planetary average of geomagnetic perturbations, which is probably the best that is currently available. However, the 3-hour cadence of K_p is a serious weakness for a SAPS model parameter, as significant temporal variations of SAPS can be observed on time scales of 90 minutes or less (e.g., *Goldstein et al.* [2003b]). It should be investigated whether some combination of two or more higher-time-resolution indices, tailored to measure the SAPS effect more directly, might better serve to parameterize a future SAPS model.

From this first attempt to create an analytical SAPS model it is clear that the SAPS effect itself needs to be better characterized. The work of *Foster and Vo* [2002] is currently the only published study of average SAPS properties, but it is not an ideal basis for the creation of a SAPS model. For example, the MLT dependence of the latitudinal thickness of the SAPS flow channel needs to be better characterized (using more than two MLTs), and its dependence on K_p also must be determined. We expect that when better characterization of SAPS properties becomes available, the functional form we have presented will be useful in constructing a refined SAPS model.

The SAPS effect is the result of a dynamic, coupled response of the inner magnetosphere and ionosphere. In truth, only a self-consistent model can hope to truly capture such an effect. In addition, our approach has relied on an equipotential formulation that inherently excludes the effect of time-variable magnetic fields. Despite these obvious deficiencies (and those listed above), the K_p-parameterized model did a credible job of reproducing the plasmaspheric effects of SAPS, both on a case-by-case basis, and in an average sense.

5. Conclusions

We have presented a first attempt at a general-use equatorial model of the subauroral polarization stream (SAPS) electric potential. Unlike the ad-hoc SAPS potential of *Goldstein et al.* [2003b], which was optimized for a single case study, our SAPS model is parameterized by K_p (valid for K_p between 4 and 7), based on the average SAPS properties reported by *Foster and Vo* [2002]. We performed two tests of the model. The first test was a case study of the 2 June 2001 erosion event; in this test, our general-use model reproduced the results of *Goldstein et al.* [2003b] for this event. The second test was to apply our model to 13 events during the period 1 April through 31 May 2001. From comparison between simulation results and plasmapause data obtained by the IMAGE extreme ultraviolet (EUV) imager for these 13 events, it is clear that inclusion of the SAPS model improves simulation performance. The K_p-based SAPS model should contribute to an improved understanding of the inner magnetospheric electric field, and help in the prediction of the location and shape of plasmaspheric plumes, which play an important role in magnetospheric dynamics. It may also provide a useful functional form for future work in constructing a more refined SAPS model.

Acknowledgments.
We are grateful to N. Ness, C. Smith, D. McComas, and the ACE science center for the excellent ACE data. This project was supported by the NASA Sun-Earth Connections Guest Investigator program under NAG5-12787 (JG), and by the NASA IMAGE Mission under NAS5-96020 (JG, JLB, BRS). We thank J. C. Foster for providing some unpublished average SAPS data. JG is grateful to P. C. Anderson and J. C. Foster for enjoyable and informative discussions.

References

Anderson, P. C., D. L. Carpenter, K. Tsuruda, T. Mukai, and F. J. Rich (2001), Multisatellite observations of rapid subauroral ion drifts (SAID), *J. Geophys. Res.*, *106*, 29585.

Baker, D. N., S. G. Kanekal, X. Li, S. P. Monk, J. Goldstein, and J. L. Burch (2004), An extreme distortion of the Van Allen belt arising from the 'Halloween' solar storm in 2003, *Nature*, *432*, 878, doi:10.1038/nature03116.

Burke, W. J., et al. (1998), Electrodynamics of the inner magnetosphere observed in the dusk sector by CRRES and DMSP during the magnetic storm of June 4–6, 1991, *J. Geophys. Res.*, *103*, 29399.

Carpenter, D. L., and J. Lemaire (1997), Erosion and recovery of the plasmasphere in the plasmapause region, *Space Sci. Rev.*, *80*, 153.

Dungey, J. W. (1961), Interplanetary magnetic field and the auroral zones, *Phys. Rev. Lett.*, *6*, 47.

Foster, J. C., and W. J. Burke (2002), SAPS: A new categorization for sub-auroral electric fields, *EOS Trans. AGU*, *83*, 393.

Foster, J. C., and H. B. Vo (2002), Average characteristics and activity dependence of the subauroral polarization stream, *J. Geophys. Res.*, *107*(A12), 1475, doi:10.1029/2002JA009409.

Goldstein, J., and B. R. Sandel (2005), The global pattern of evolution of plasmaspheric drainage plumes, in *Global Physics of the Coupled Inner Magnetosphere*, edited by M. Schulz, H. Spence, and J. L. Burch, American Geophysical Union, Washington, D. C., in press.

Goldstein, J., B. R. Sandel, W. T. Forrester, and P. H. Reiff (2003a), IMF-driven plasmasphere erosion of 10 July 2000, *Geophys. Res. Lett.*, *30*(3), doi:10.1029/2002GL016478.

Goldstein, J., B. R. Sandel, P. H. Reiff, and M. R. Hairston (2003b), Control of plasmaspheric dynamics by both convection and sub-auroral polarization stream, *Geophys. Res. Lett.*, *30*(24), 2243, doi:10.1029/2003GL018390.

Goldstein, J., M. Spasojević, P. H. Reiff, B. R. Sandel, W. T. Forrester, D. L. Gallagher, and B. W. Reinisch (2003c), Identifying the plasmapause in IMAGE EUV data using IMAGE RPI in situ steep density gradients, *J. Geophys. Res.*, *108*(A4), 1147, doi:10.1029/2002JA009475.

Goldstein, J., B. R. Sandel, M. F. Thomsen, M. Spasojević, and P. H. Reiff (2004), Simultaneous remote-sensing and in situ observations of plasmaspheric drainage plumes, *J. Geophys. Res.*, *109*, A03202, doi:10.1029/2003JA010281.

Lemaire, J. F., and K. I. Gringauz (1998), *The Earth's Plasmasphere*, Cambridge University Press, Cambridge.

Maynard, N. C., and A. J. Chen (1975), Isolated cold plasma regions: Observations and their relation to possible production mechanisms, *J. Geophys. Res.*, *80*, 1009.

Roelof, E. C., and A. J. Skinner (2000), Extraction of ion distributions from magnetospheric ENA and EUV images, *Space Sci. Rev.*, *91*, 437.

Sandel, B. R., R. A. King, W. T. Forrester, D. L. Gallagher, A. L. Broadfoot, and C. C. Curtis (2001), Initial results from the IMAGE extreme ultraviolet imager, *Geophys. Res. Lett.*, *28*, 1439.

Spasojević, M., H. U. Frey, M. F. Thomsen, S. A. Fuselier, S. P. Gary, B. R. Sandel, and U. S. Inan (2004), The link between a detached subauroral proton arc and a plasmaspheric plume, *Geophys. Res. Lett.*, *31*, L04803, doi: doi:10.1029/2003GL018389.

Stern, D. P. (1975), The motion of a proton in the equatorial magnetosphere, *J. Geophys. Res.*, *80*, 595.

Stone, E. C., A. M. Frandsen, R. A. Mewaldt, E. R. Christian, D. Margolies, J. F. Ormes, and F. Snow (1998), The Advanced Composition Explorer, *Space Sci. Rev.*, *86*, 1.

Tsyganenko, N. A. (1989), A magnetospheric magnetic field model with a warped tail current sheet, *Planet. Space Sci.*, *37*, 5.

Volland, H. (1973), Semiempirical model of large-scale magnetospheric electric fields, *J. Geophys. Res.*, *78*, 171.

J. Goldstein, J. L. Burch, Southwest Research Institute, 6220 Culebra Road, San Antonio, TX 78228 USA (jgoldstein@swri.edu)

B. R. Sandel, Lunar and Planetary Lab, University of Arizona, Tucson, AZ 85721 USA

(Received ______________________.)